






Ultrafast optogenetic stimulation of the auditory pathway by targeting-optimized Chronos

Daniel Keppeler^{1,2,‡} , Ricardo Martins Merino^{2,3,4,5,‡}, David Lopez de la Morena^{1,2,6,‡} , Burak Bali^{1,2,7,§}, Antoine Tarquin Huet^{1,3,6,§}, Anna Gehrt^{1,8}, Christian Wrobel^{1,8}, Swati Subramanian^{1,2}, Tobias Dombrowski^{1,†}, Fred Wolf^{4,5,8,9,10}, Vladan Rankovic^{1,7,*} , Andreas Neef^{3,4,10,**}  & Tobias Moser^{1,2,3,5,6,8,11,***} 

Abstract

Optogenetic tools, providing non-invasive control over selected cells, have the potential to revolutionize sensory prostheses for humans. Optogenetic stimulation of spiral ganglion neurons (SGNs) in the ear provides a future alternative to electrical stimulation used in cochlear implants. However, most channelrhodopsins do not support the high temporal fidelity pertinent to auditory coding because they require milliseconds to close after light-off. Here, we biophysically characterized the fast channelrhodopsin Chronos and revealed a deactivation time constant of less than a millisecond at body temperature. In order to enhance neural expression, we improved its trafficking to the plasma membrane (Chronos-ES/TS). Following efficient transduction of SGNs using early postnatal injection of the adeno-associated virus AAV-PHP.B into the mouse cochlea, fiber-based optical stimulation elicited optical auditory brainstem responses (oABR) with minimal latencies of 1 ms, thresholds of 5 μ J and 100 μ s per pulse, and sizable amplitudes even at 1,000 Hz of stimulation. Recordings from single SGNs demonstrated good temporal precision of light-evoked spiking. In conclusion, efficient virus-mediated expression of targeting-optimized Chronos-ES/TS achieves ultrafast optogenetic control of neurons.

Keywords channelrhodopsin; cochlear implant; neural coding; spiral ganglion; trafficking

Subject Categories Methods & Resources; Neuroscience

DOI 10.15252/embj.201899649 | Received 16 April 2018 | Revised 25 September 2018 | Accepted 28 September 2018 | Published online 5 November 2018

The EMBO Journal (2018) 37: e99649

See also: E Ronzitti *et al* (December 2018)

Introduction

Since the discovery of channelrhodopsins (ChRs, Nagel *et al*, 2002, 2003) and the application of these light-gated ion channels for controlling excitable cells (Boyden *et al*, 2005), the concept of optogenetics has revolutionized the life sciences (Adamantidis *et al*, 2015; Kim *et al*, 2017). Application of optogenetics to restore sensory function in the immune-privileged eye and the ear is thought to have a fair chance of clinical translation (Sahel & Roska, 2013; Jeschke & Moser, 2015). Indeed, AAV-mediated optogenetics for vision restoration has recently entered a first clinical trial in a dose-finding effort (RST-001 Phase I/II Trial for Advanced Retinitis Pigmentosa—Full Text View—ClinicalTrials.gov). While neural coding of visual information can likely be achieved with ChRs that deactivate within several milliseconds (Busskamp *et al*, 2012), faster ChRs are required for sound coding in spiral ganglion neurons of the ear (SGNs) that spike at hundreds of Hz with sub-millisecond precision (Jeschke & Moser, 2015).

If such ultrafast optogenetic control of neural activity was available, it would serve auditory research and could fuel the development of future optical cochlear implants (oCIs). Clinically, this is highly relevant as approximately 466 million people—over 5% of the world's population—suffer from a disabling hearing impairment (WHO, 2008) and we are still lacking causal therapies for the most

- 1 Institute for Auditory Neuroscience and InnerEarLab, University Medical Center Göttingen, Göttingen, Germany
- 2 Göttingen Graduate School for Neurosciences and Molecular Biosciences, University of Göttingen, Göttingen, Germany
- 3 Biophysics of Neural Computation Group, Bernstein Center for Computational Neuroscience Göttingen, Göttingen, Germany
- 4 Neurophysics Group, Max Planck Institute for Dynamics and Self-Organization, Göttingen, Germany
- 5 Max Planck Institute for Experimental Medicine, Göttingen, Germany
- 6 Auditory Neuroscience and Optogenetics Laboratory, German Primate Center, Göttingen, Germany
- 7 Restorative Cochlear Genomics Group, German Primate Center, Göttingen, Germany
- 8 Collaborative Research Center 889, University of Göttingen, Göttingen, Germany
- 9 Bernstein Center for Computational Neuroscience, Göttingen, Germany
- 10 Campus Institute for Dynamics of Biological Networks, Göttingen, Germany
- 11 Center for Nanoscale Microscopy and Molecular Physiology of the Brain, Göttingen, Germany

*Corresponding author. Tel: +49 551 3851 209; E-mail: vrankovic@dpz.eu

**Corresponding author. Tel: +49 551 3961 107; E-mail: andreas@nld.ds.mpg.de

***Corresponding author. Tel: +49 551 3963 070; E-mail: tmoser@gwdg.de

‡These authors contributed equally to this work

§These authors contributed equally to this work

† Present address: Department of Otorhinolaryngology, Head and Neck Surgery, St. Elisabeth Hospital, Ruhr University Bochum, Bochum, Germany

common form, sensorineural hearing impairment. Consequences are impaired communication, often social isolation, depression, and reduction in professional capabilities. As of today, partial restoration of auditory function by hearing aids and electrical CIs (eCI) represents the options of choice for rehabilitation in sensorineural hearing impairment, which results from cochlear dysfunction or degeneration. The eCI bypasses dysfunctional or lost cochlear hair cells via direct electric stimulation of SGNs and, with most of the approximately 500,000 users achieving open speech comprehension, is considered the most successful neuroprosthesis (Zeng, 2017; Lenarz, 2018). Nonetheless, there is an urgent need for further improvement of the CI. The biggest bottleneck of the eCI is the poor spectral resolution of coding that arises from the widespread of current around each electrode contact (Kral *et al*, 1998). Using light for stimulation in oCI is one of the present developments to improve spectral coding by CIs, as light can be better spatially confined than electric current (e.g., Richter *et al*, 2011; Hernandez *et al*, 2014). One of the implementations used optogenetic stimulation of SGNs for a first proof-of-principle study on activation of the auditory pathway up to the midbrain (inferior colliculus, IC), demonstrating a lower spread of cochlear excitation for fiber-based oCI than for monopolar eCI (Hernandez *et al*, 2014). However, the temporal fidelity of ChR2-mediated optogenetic control of SGN firing seemed limited; auditory brainstem responses broke down even below 100 Hz of stimulation. Higher temporal fidelity of optogenetic SGN stimulation might be achieved when using faster ChRs such as Chronos (Klapoetke *et al*, 2014), the newly engineered Chronos mutant ChROME (Mardinly *et al*, 2018), or fast Chrimson mutants (Mager *et al*, 2018).

Therefore, characterizing and optimizing fast ChRs are of great importance for fast-spiking neurons in the auditory system, but also in the somatosensory system, cerebellum, and a wide range of inhibitory circuits. Here, we targeted Chronos, the fastest ChR reported so far, and first dissected its gating by patch-clamp recordings of photocurrents. Toward its application for optogenetic stimulation of mouse SGNs, we optimized Chronos, the viral vector and virus injection approach for achieving high plasma membrane expression. As described for another opsin (Gradinaru *et al*, 2010), we appended sequences for improved exit from the endoplasmic reticulum (ES) (Ma *et al*, 2001; Stockklausner *et al*, 2001) and trafficking to the plasma membrane (TS) (Hofherr *et al*, 2005) to Chronos (Chronos-ES/TS) and performed postnatal injections of AAV-PHP.B serotype (Deverman *et al*, 2016), which drove highly efficient Chronos-ES/TS expression. We demonstrate by recordings of oABR and single SGN firing that Chronos-ES/TS enables ultrafast stimulation of the auditory pathway.

Results

Chronos undergoes sub-millisecond on/off transitions at 36°C

The kinetic properties of ChRs are best studied in cells with little background conductance to characterize the light-induced conductance in isolation. To this end, we used human embryonic kidney cells 293T (HEK-293T cells) expressing Chronos or ChR2 (Materials and Methods). We clamped the membrane voltage to -60 mV where any light-induced change in the conductance is then linearly reflected in a change of the pipette current. First, we compared gating kinetics

of ChR2 and Chronos at a low light intensity of 0.27 mW mm⁻², far below the half-maximal activation. At 22°C, we found activation and deactivation time constants (mean \pm SEM) of $\tau_{\text{act}} = 4.9 \pm 0.3$ ms, $\tau_{\text{deact}} = 9.4 \pm 1.0$ ms ($n = 6$) for ChR2 and $\tau_{\text{act}} = 1.5 \pm 0.1$ ms, $\tau_{\text{deact}} = 3.0 \pm 0.2$ ms ($n = 21$) for Chronos (Fig 1A). When increasing the temperature to 36°C, activation and deactivation accelerated, with $\tau_{\text{act}} = 0.58 \pm 0.02$ ms and $\tau_{\text{deact}} = 0.76 \pm 0.05$ ms ($n = 6$), Chronos reached the sub-millisecond range, while ChR2 gating kinetics, $\tau_{\text{act}} = 2.3 \pm 0.1$ ms, $\tau_{\text{deact}} = 3.0 \pm 0.3$ ms ($n = 6$ and 5, respectively), at 36°C were comparable to the values achieved by Chronos at 22°C. Hence, already at such a low light intensity, Chronos, but not ChR2, activation and deactivation should permit signal transmission with a bandwidth of several hundred Hertz. Probing the frequency bandwidth directly by applying light chirps, Chronos confers a much higher bandwidth compared to ChR2 (Fig 1B). The gain of chirp responses could be very well characterized by a single cutoff frequency of 24 Hz and 86 Hz for ChR2 and Chronos, respectively, at 22°C and 63 Hz and 150 Hz at 36°C (Fig 1C).

Improving the plasma membrane expression of Chronos

The above biophysical characterization had indicated Chronos as a strong candidate for optogenetic stimulation of SGNs with the required high temporal fidelity, provided sufficient plasma membrane expression can be achieved. Recent studies have shown that adding ER export and trafficking signals, isolated from a vertebrate inward rectifier potassium channel, to the cytoplasmic C terminus of opsins promote their plasma membrane expression (Gradinaru *et al*, 2010). Hence, we added these sequences, here nick-named ES (Export Signal) and TS (Trafficking Signal), sandwiching EYFP, to Chronos (Chronos-ES/TS, Fig 2A). We first compared expression of Chronos-ES/TS and Chronos in HEK-293T cells transfected with the respective pAAV plasmid by immunocytochemistry. Using confocal and stimulated emission depletion (STED) microscopy, we found a preferentially peripheral, likely plasmalemmal, localization of Chronos-ES/TS with some intracellular signal most likely arising from the Golgi, while the original Chronos construct was more diffusely distributed throughout the extranuclear intracellular space (Fig 2B–D). We quantified the cellular distribution of the opsin by line profile analysis (Fig 2C) and found a significantly greater peripheral than central immunofluorescence for Chronos-ES/TS when compared to the original Chronos construct (Fig 2C and D). The larger variance of the ratio of membrane and intracellular fluorescence for Chronos-ES/TS (Fig 2D) is likely explained by dividing by the relatively low, yet varying intracellular abundance of the opsin. In summary, the data suggest improved trafficking to the plasma membrane of Chronos-ES/TS.

Similar findings were also obtained in hippocampal neurons in culture transduced by AAV2/6 or AAV-PHP.B (Fig 3). This indicates that neurons, too, struggle to traffic Chronos to the plasma membrane and that this can be alleviated when adding the ES and TS signals, at least when tested in culture.

AAV-mediated expression of Chronos and Chronos-ES/TS in mouse SGNs

Next, we turned to expression of Chronos in mouse SGNs *in vivo* and, once more, compared the original Chronos and Chronos-ES/

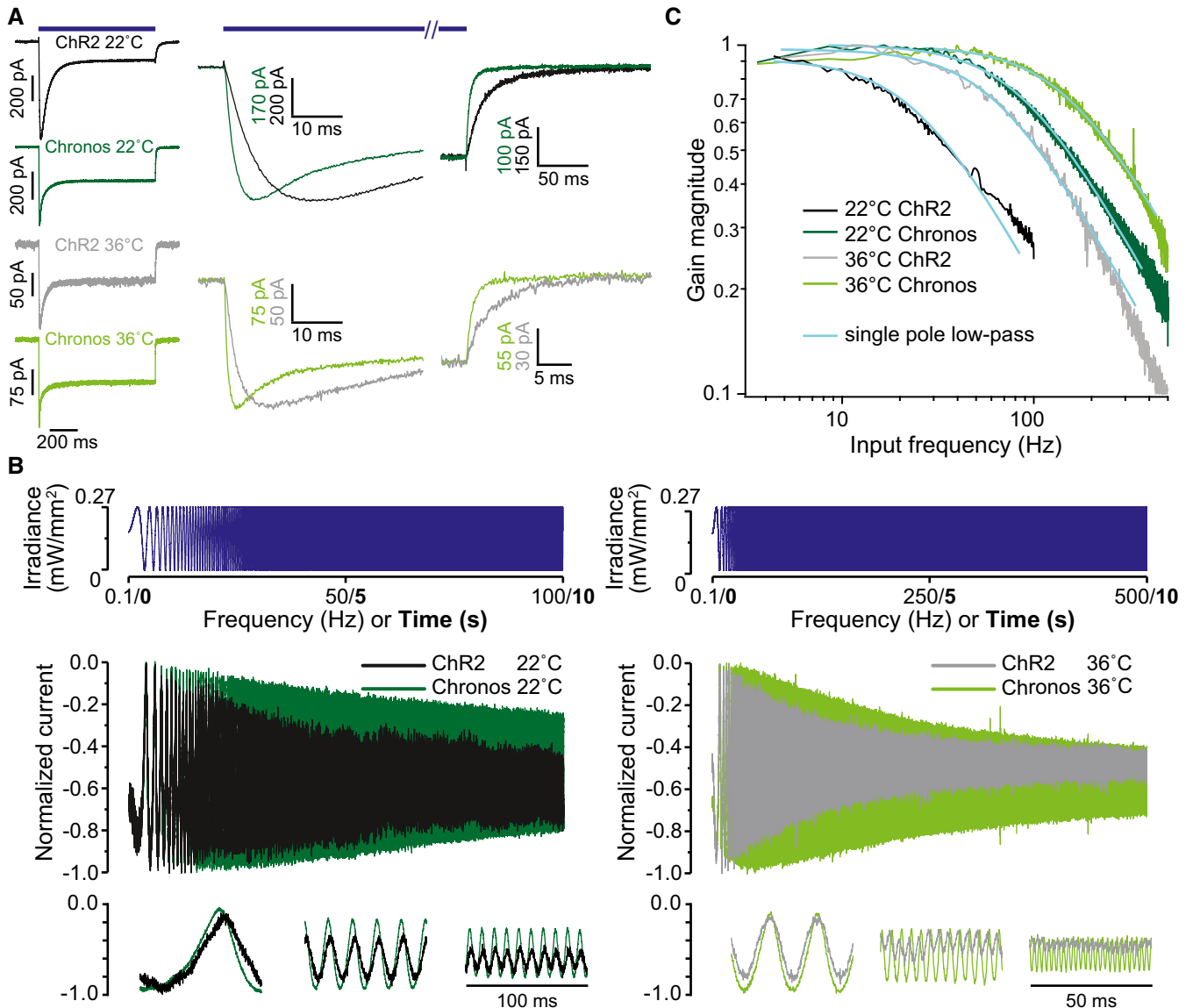


Figure 1. Chronos mediates fast light-driven currents.

A One-second-long light pulses (LED centered 480 nm, 0.27 mW/mm²) elicit current responses in HEK-293T cells expressing ChR2 and Chronos, tested at 22 and 36°C. Right panels show activation and deactivation at higher time resolution.

B A quasi-periodic chirp stimulus is used to directly probe the bandwidth of Chronos- and ChR2-mediated photocurrents in HEK-293T cells. Top: stimulus, middle: full response, bottom: sections from the beginning, middle, and end of the response. Note the substantially larger frequency range over which Chronos currents follow the light stimulus. At 36°C, this range is extended even further.

C Analysis of the chirp responses of HEK-293T cells as in (B). The current amplitude modulation is plotted against the stimulus frequency. The smooth lines represent fits to the magnitude of the transfer function of a single pole filter $\text{abs}((1 + i f/f_{\text{cut}})^{-1})$.

TS. We aimed to establish efficient AAV-mediated transduction of SGNs and employed the human synapsin promoter (hSyn, Fig 2A) that had turned out to drive efficient and specific SGN expression (Hernandez *et al*, 2014). We first followed our previous protocol using transuterine injections of AAV2/6 into the otocyst of mouse embryos at embryonic day 11.5 (Fig 4A, upper). In most of the cases, the expression of Chronos-EGFP was absent or sparse (Fig 4B, left and middle). Exceptionally we saw high expression levels (Fig 4B right). As before (Hernandez *et al*, 2014), the expression, if any, was largely limited to the SGNs of the basal

cochlear turn and was never seen in inner hair cells (Fig 4B right, inset).

Next, we moved on to early postnatal injections (Fig 4A, middle and lower, postnatal day 5–7) into the cochlea via the round window, which had proven highly successful for transduction of hair cells (e.g., Akil *et al*, 2012; Jung *et al*, 2015). We employed AAV-PHP.B, a novel AAV serotype (Deverman *et al*, 2016) with improved efficiency of neural transduction, for expression of Chronos-ES/TS and Chronos (hSyn promoter, comparable titers, 10¹² GC/ml) in SGNs. Twelve out of 12 AAV-PHP.B-injected mice

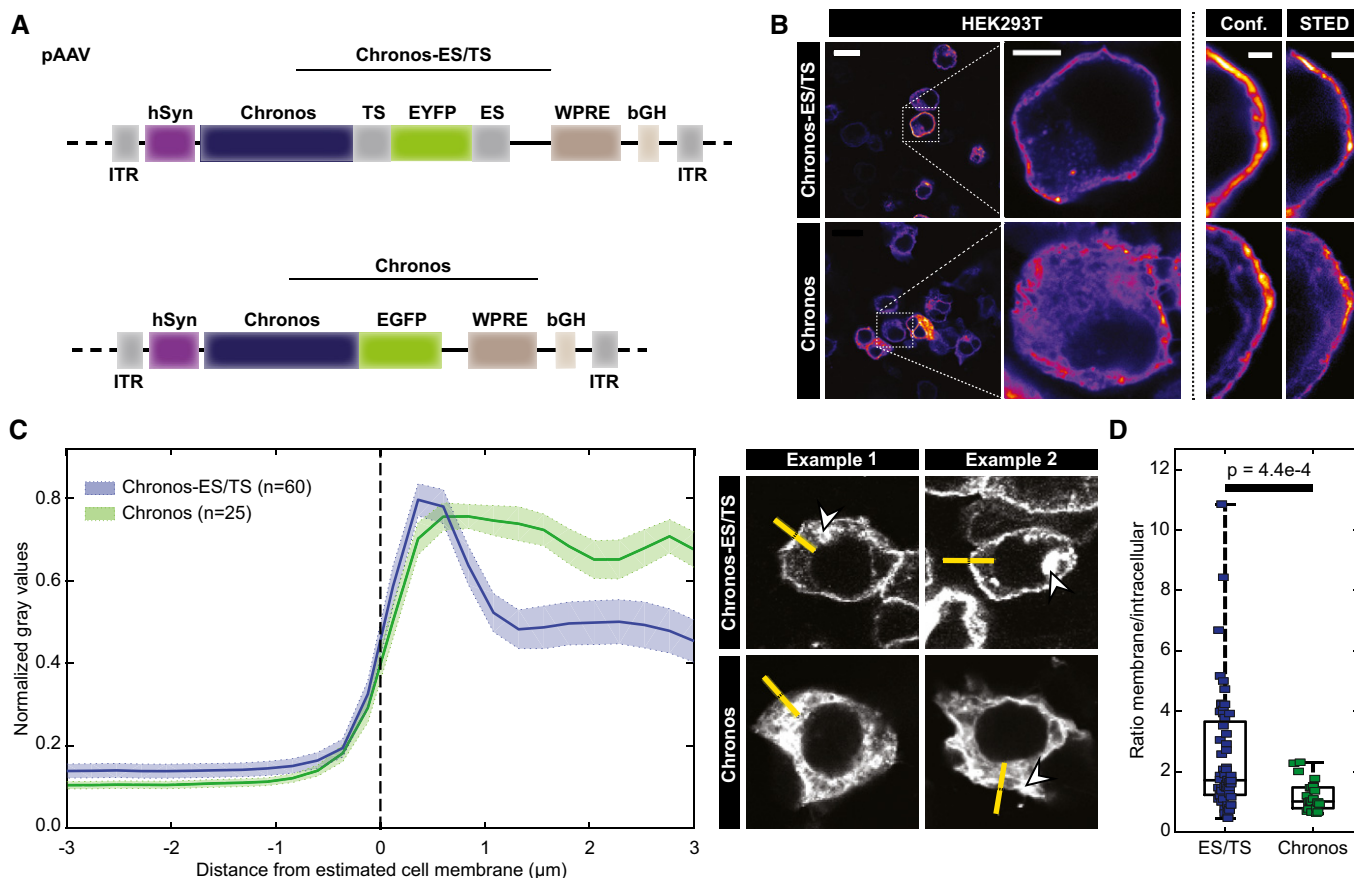


Figure 2. Optimizing membrane expression of Chronos by adding ER-exit and trafficking signals: HEK-293T cells.

A pAAV vector used in the study Chronos with a trafficking signal (TS), EYFP and ER export (ES) Chronos-ES/TS (upper) or containing the original Chronos-EGFP (Klapoetke *et al*, 2014; lower). In each, expression was driven by the human synapsin promoter (hSyn) and enhanced by the Woodchuck hepatitis virus posttranslational regulatory element (WPRE) and bovine growth hormone (bGH) polyadenylation signal (bGH poly A) sequences. ITR: inverted terminal repeats.

B Confocal and STED section of representative HEK-293T cells transfected with Chronos-ES/TS (upper) and Chronos (lower) and immunolabeled for FP: membranous labeling is more obvious for Chronos-ES/TS. Scale bars: 10, 5 and 2 μm for left, middle, and right panels.

C Peak-normalized line profiles (7.5 μm) centered on the estimated membrane of HEK-293T cells expressing Chronos-ES/TS (blue) or Chronos (green) as in (B): mean \pm SEM. Chronos-ES/TS-expressing cells showed a clear peripheral, likely membrane peak, which is missing in Chronos-expressing cells. Right panels show exemplary line profile placements (yellow). One line per cell was placed perpendicular and centered to cell edge, aiming at sufficient intracellular coverage and avoiding fluorescent aggregates (arrowheads). N corresponds to analyzed cells (1 sample/cell).

D Box and whisker plot ratio of maximal membrane and maximal cytoplasmic fluorescence of immunolabeled HEK-293T cells expressing Chronos-ES/TS or Chronos: Mann-Whitney *U*-test showed significantly higher ratio in Chronos-ES/TS cells demonstrating an improved membrane expression of Chronos-ES/TS (P -value = 4.4e-4). The horizontal line within the box indicates the median, boundaries of the box indicate the 0.25- and 0.75-percentile, and the whiskers indicate the highest and lowest values of the results. Squares: individual data points. For details on membranous and cytoplasmic area, see Materials and Methods section.

showed substantial SGN transduction in immunohistochemistry for Chronos-ES/TS and 9 out of 9 for Chronos. Postnatal injection of AAV-PHP.B drove strong expression of Chronos-ES/TS across all cochlear turns (Fig 4C). Similar to HEK-293T cells and hippocampal neurons *in vitro*, Chronos-ES/TS localized preferentially peripheral, likely plasmalemmal in SGNs *in vivo*, while the original Chronos construct was more diffusely distributed throughout the cell (Fig 4D). Once again, we quantified the cellular distribution of the opsin by line profile analysis (Fig 4E) and found a significantly greater peripheral than central immunofluorescence for Chronos-ES/TS when compared to the original Chronos construct (Fig 4E, $P = 4.1e-5$). The difference can be appreciated by the 0.56 μm more intracellular 50% FP immunofluorescence for Chronos. We note that the cytosolic parvalbumin immunofluorescence allowed a

better estimation of the cell border which was independent of the opsin expression, both advantageous when compared to HEK-293T cell analysis (Fig 2). Despite some differences in absolute numbers between both analyses, which are not unexpected given the different cell types, means of transfection and analysis method, both support the main observation: improved relative plasma membrane abundance of Chronos-ES/TS.

When analyzing the transduction rates in the injected (left) and non-injected (right) cochleae, we confirmed robust SGN transduction across all turns of the injected cochlea for both Chronos-ES/TS and Chronos (Fig 4F). We note that the counterstain for parvalbumin- α , used for AAV-PHP.B-injected ears, is a more general marker of SGNs than calretinin, used for AAV2/6 injected ears, which is present only in a subset of SGNs. Therefore, if anything, we would

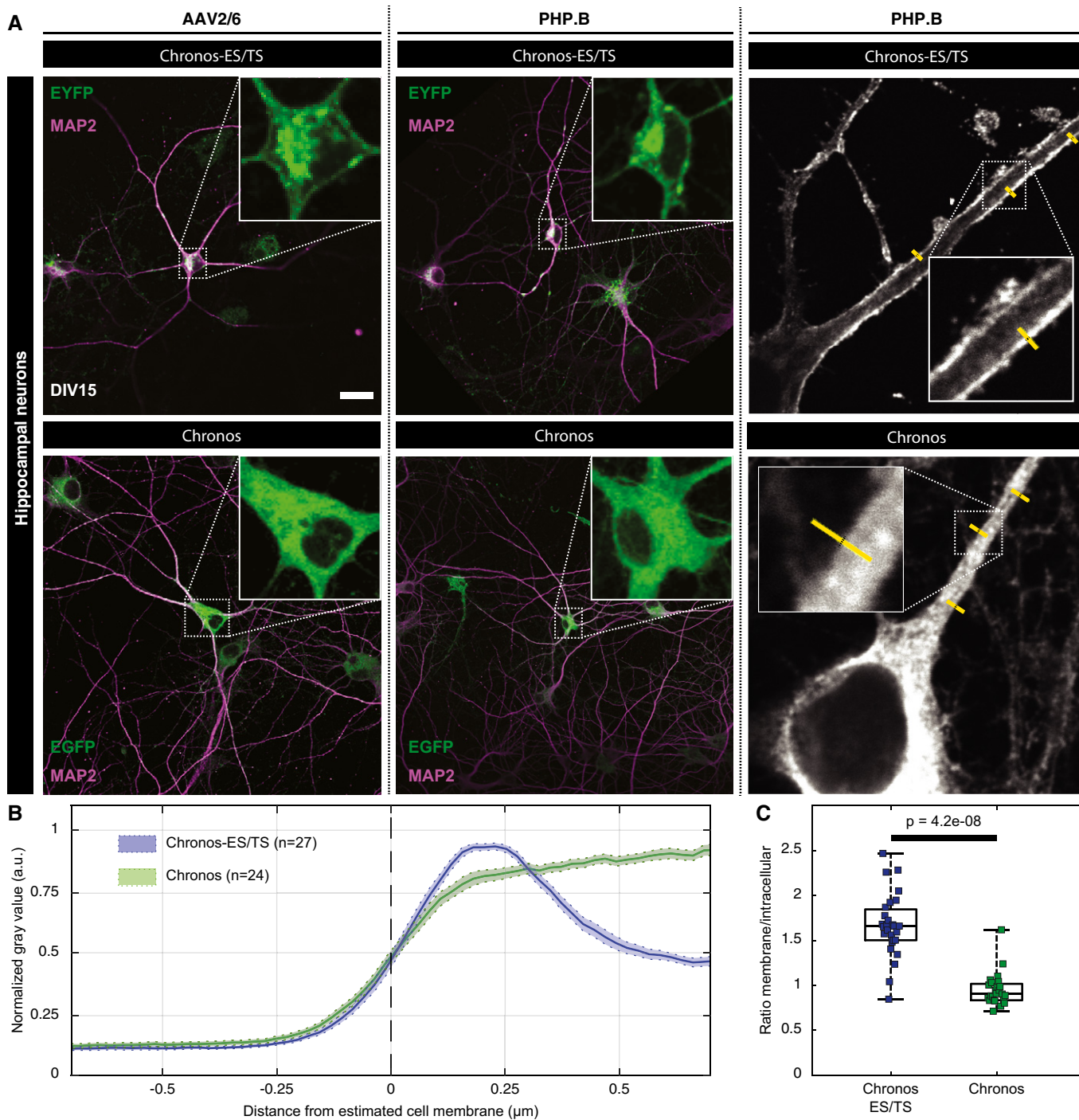


Figure 3. Improved membrane expression of optimized Chronos-ES/TS in hippocampal neurons.

A Hippocampal neurons infected at DIV 10 with two different versions of Chronos show very distinct expression patterns. Neurons infected with Chronos-ES/TS (upper panels) either using AAV2/6 (left) or PHP.B virus (middle) show very specific plasma membrane expression in somatic regions and proximal dendrites. Infection of neurons with Chronos (lower panels) either using AAV2/6 (left) or AAV-PHP.B (middle) showed more intracellular opsin abundance. Right panels show exemplary line profile placement (yellow). Scale bar: 50 μm applies to all panels.

B Peak-normalized line profiles (1.5 μm) centered on the outer cell edge of AAV-PHP.B transduced hippocampal proximal dendrites expressing Chronos-ES/TS (blue) or Chronos (green) as in (A): mean \pm SEM. Chronos-ES/TS-expressing cells showed a clear peripheral, likely plasmalemmal peak, which is missing in Chronos-expressing cells.

C Box and whisker plot of the ratio of maximal membrane and maximal intracellular fluorescence of immunolabeled hippocampal neurons expressing Chronos-ES/TS or Chronos: Mann-Whitney *U*-test showed significantly higher ratio in Chronos-ES/TS cells demonstrating an improved membrane expression of Chronos-ES/TS (*P*-value = 4.2e-8). The horizontal line within the box indicates the median, boundaries of the box indicate the 0.25- and 0.75-percentile, and the whiskers indicate the highest and lowest values of the results. Squares: individual data points. For details on membranous and cytoplasmic area, see Materials and Methods section.

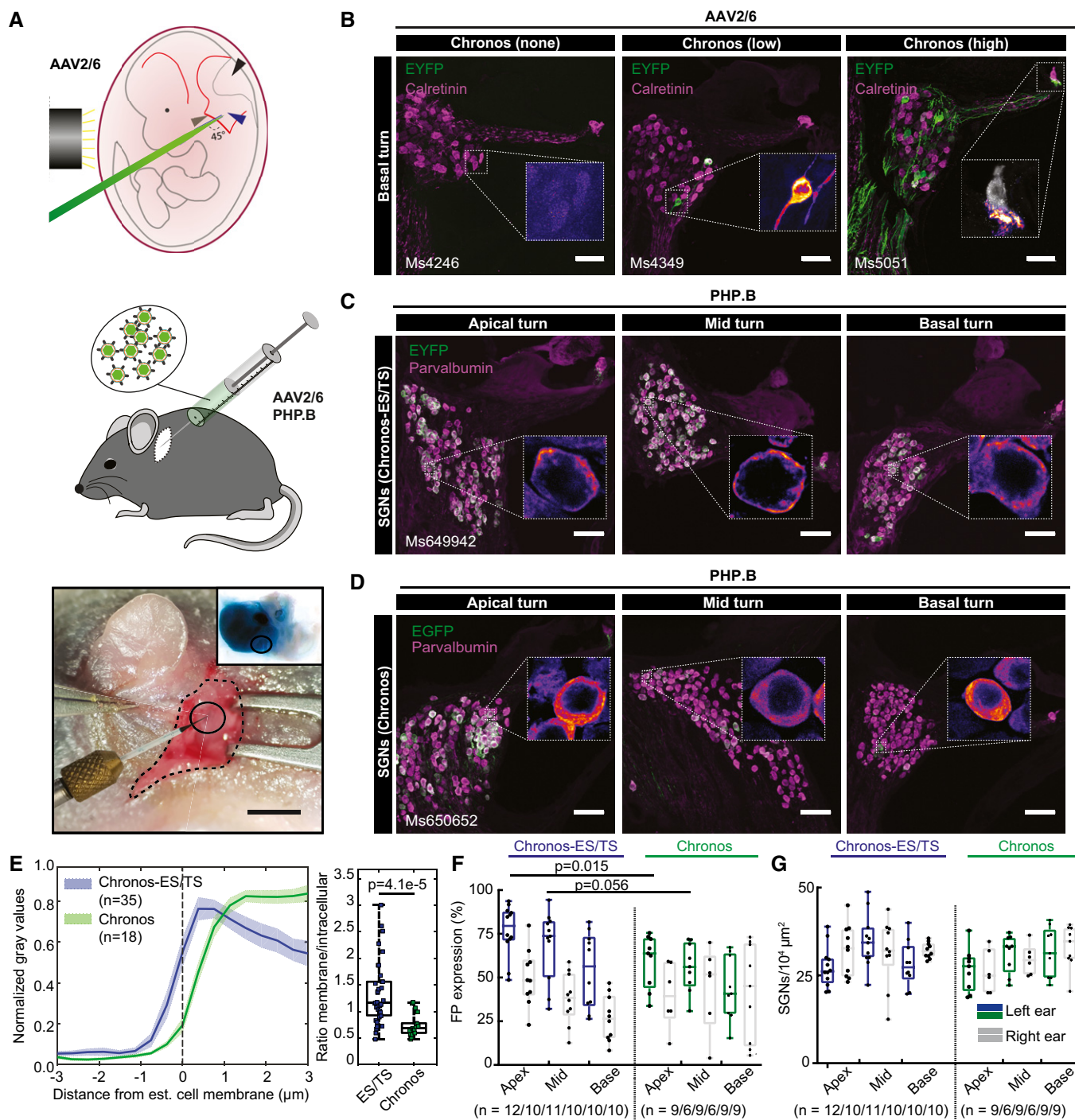


Figure 4.

have been prone to overestimate the transduction rate for AAV2/6 injected ears, which, however, was very low. Interestingly, for both cases of AAV-PHP.B injection, we also found substantial expression in the contralateral, non-injected cochleae, indicating spread of virus in the specific conditions of pressure injection into the scala tympani of the early postnatal cochlea. This spread likely occurred via the cochlear aqueduct and/or the endolymphatic ducts and the cerebrospinal fluid space (Lalwani *et al*, 1996). The density of SGNs in the injected as well as in non-injected ears was comparable

(Fig 4G). The injected mice behaved normal as concluded from routine animal observation.

Chronos-mediated optogenetic neural stimulation of the auditory pathway: transuterine injections of AAV2/6

We performed acute recordings of oABRs using fiber-coupled laser stimulation 4–12 weeks after AAV injection. Following posterior tympanotomy, we inserted a 50-μm optical fiber through the round

Figure 4. Establishing efficient expression of Chronos in SGNs: use of Chronos-ES/TS, potent AAV-PHP.B, and postnatal mode of AAV injection.

- A Upper panel: schematic representation of the viral injection into the embryonic otocyst (left: black cylinder marks the light guide used to trans-illuminate the embryo in the uterus after mobilization from the abdominal cavity, green: micropipette filled with fast green-colored AAV suspension). Middle panel: schematic representation of AAV injection into the postnatal cochlea via the round window (RW). Lower panel: surgical situs of a p7 mouse with retroauricular incision, graphical aid encircles the injection site). Inset shows *ex vivo* cochlea just after AAV injection via RW. Scale bar: 2 mm.
- B Maximum projection of confocal images of immunolabeled mid-modiolar cochlear cryosections (exemplary sections of basal turn) of embryonically AAV2/6-Chronos-injected mice collected at 4 weeks of age. EYFP (green) marks transduced SGNs, calretinin (magenta) was used as generic marker of SGNs, scale bar: 50 μ m. In the inset, color code for EYFP channel was changed to fire (EYFP). Left panel: most common, non-expressing example, inset shows zoom of negative SGNs. Middle panel: occasional, sparsely expressing example, inset: one out of two positive SGNs. Right panel: rare, highly expressing example, inset: negative inner hair cell (calretinin in gray), exclusive localization of EYFP in the SGN boutons and fibers.
- C Postnatally AAV-PHP.B-Chronos-ES/TS-injected mouse (see (B) except where stated differently). EYFP (green) marks transduced SGNs, parvalbumin (magenta) was used as generic marker of SGNs, scale bar: 50 μ m. High transduction rate, good membrane expression. In inset, color code for the green channel was changed to fire for better visualization. Similar to (B).
- D Postnatally AAV-PHP.B-Chronos-injected mouse (see (C) except where stated differently). Substantial SGN transduction, poor membrane expression.
- E Line profile analysis of FP immunofluorescence across the membrane of SGN somata. Traces were centered at the transition from high to low parvalbumin immunofluorescence as a proxy of plasma membrane location. Left panel: clear membrane abundance in Chronos-ES/TS (blue, mean \pm SEM), but mostly intracellular localization in Chronos (green, mean \pm SEM). Right panel: Box and whisker plot of the ratio of maximal membrane and maximal intracellular FP fluorescence for Chronos-ES/TS (left) and Chronos (right): stronger relative membrane expression in Chronos-ES/TS (Mann–Whitney *U*-test, *P*-value = 4.1e-5). Squares: individual data points. For details on membranous and cytoplasmic area, see Materials and Methods section.
- F Box and whisker plot of the fraction of FP-positive SGNs (transduced out of all parvalbumin-positive SGNs) for the apical, middle, and basal cochlear turn of the injected ear (colored) and contralateral, non-injected (gray) ear of Chronos-ES/TS-AAV-PHP.B and Chronos-AAV-PHP.B mice. Points: individual animals plotted on top; *n* refers to number of cochleae studied. The horizontal line within the box indicates the median, boundaries of the box indicate the 0.25- and 0.75-percentile, and the whiskers indicate the highest and lowest values of the results.
- G Box and whisker of the SGN density for the apical, middle, and basal cochlear turn of the injected (colored) ear and the contralateral, non-injected (gray) ear (as in (F)). No significant differences between Chronos and Chronos-ES/TS or between injected and non-injected ear. Points: individual animals plotted on top; *n* refers to number of cochleae studied.

window (RW) to project the light of a blue laser ($\lambda = 473$ nm) onto the SGNs. When oABRs were present (Fig EV1), we typically found three to five oABR peaks, which likely reflected the synchronous activation of Chronos-expressing SGNs (first peak) and downstream auditory pathway (subsequent peaks). Transuterine injections of AAV2/6-Chronos did not generally support oABRs; only 3 out of dozens of injected mice (including 2 different AAV2/6 produces) showed oABRs. In these positive mice, oABR grew in amplitude and showed shorter latencies when increasing radiant flux (see inset of Fig EV1).

Chronos-ES/TS enables ultrafast optogenetic stimulation of the auditory pathway: oABRs

Postnatal injection of AAV-PHP.B reliably achieved high transduction rates (Fig 4), which enabled oABRs in 19 out of 20 AAV-PHP.B-Chronos-ES/TS-injected mice and 8 out of 17 AAV-PHP.B-Chronos-injected mice. Next, we performed a detailed characterization of Chronos-ES/TS-mediated optogenetic activation using oABRs and compared the results to those obtained with Chronos. oABR amplitude grew with increasing stimulus intensity (Fig 5A and B, 1-ms light pulses delivered at 10 Hz—averaged across 1,000 repetitions), while oABR latency (i.e., the time interval between the stimulus onset and the oABR P_1 wave) got shorter for Chronos-ES/TS (sign test between the threshold and highest radiant flux tested, *P*-value = 0.009) which did not reach statistical significance for Chronos (Fig 5A and C; *P*-value = 0.11). oABR thresholds and amplitudes differed between animals (shown for the first peak, P_1 - N_1 , Fig 5B). Stimuli as weak as 1.08 mW (duration: 1 ms, rate: 10 Hz—averaged across 1,000 repetitions) were sufficient to drive oABRs in one Chronos-ES/TS-injected mouse and 4.56 mW in a Chronos-injected mouse. For 1-ms light pulses delivered at 10 Hz, the average oABR threshold amounted to 6.58 ± 1.08 mW and

13.95 ± 3.52 mW for Chronos-ES/TS and Chronos, respectively (*P*-value = 0.0367, Mann–Whitney *U*-test; *n* = 13 and *n* = 8). In most animals, oABR amplitudes grew with radiant flux increasing over more than one order of magnitude (Fig 5B). The minimal latency of the first oABR peak (P_1 , Fig 5C) amounted to 0.95 ± 0.07 ms (*n* = 13) for Chronos-ES/TS and 1.26 ± 0.07 ms for Chronos (*n* = 8, *P*-value = 0.014, Mann–Whitney *U*-test).

oABRs could be elicited by light pulses as short as 20 μ s with Chronos-ES/TS and 400 μ s with Chronos (irradiance: 38 mW, rate: 10 Hz—averaged across 1,000 repetitions, Fig 5D and E). oABR amplitudes grew with pulse duration up to approximately 0.6 ms and tended to become smaller for longer pulses, possibly due to accumulating channel inactivation and/or increasing depolarization block of SGNs upon prolonged photo-depolarization (Fig 5D and E).

Next, we tested the dependence of oABRs on the stimulus rate [duration: 1 ms up 500 Hz and 0.5 ms from 500 Hz, intensity: maximum (38–43 mW)]. When increasing stimulus rate, oABR amplitudes declined (Fig 5G) and latencies prolonged (Fig 5G and I). However, in contrast to our previous reports on (i) ChR2: where potentials were found only up to 70 Hz (Hernandez *et al*, 2014) and (ii) CatCh: up to 200 Hz, and f-Chrimson: up to 250 Hz (respectively Wrobel *et al*, 2018; Mager *et al*, 2018), we could detect sizable P_1 - N_1 up to stimulus rates of 500 Hz for Chronos (Fig 5G left, H) and 1,000 Hz for Chronos-ES/TS (the highest stimulus rate tested in our experiments, Fig 5G and H). P_1 latency increased with higher stimulus rates in both cases.

Chronos-ES/TS enables ultrafast optogenetic stimulation of the auditory pathway: recordings from single putative SGNs

To further validate the Chronos-ES/TS-mediated SGN stimulation and evaluate the temporal fidelity of stimulation, we performed juxtacellular recordings from auditory nerve fibers (central axon of

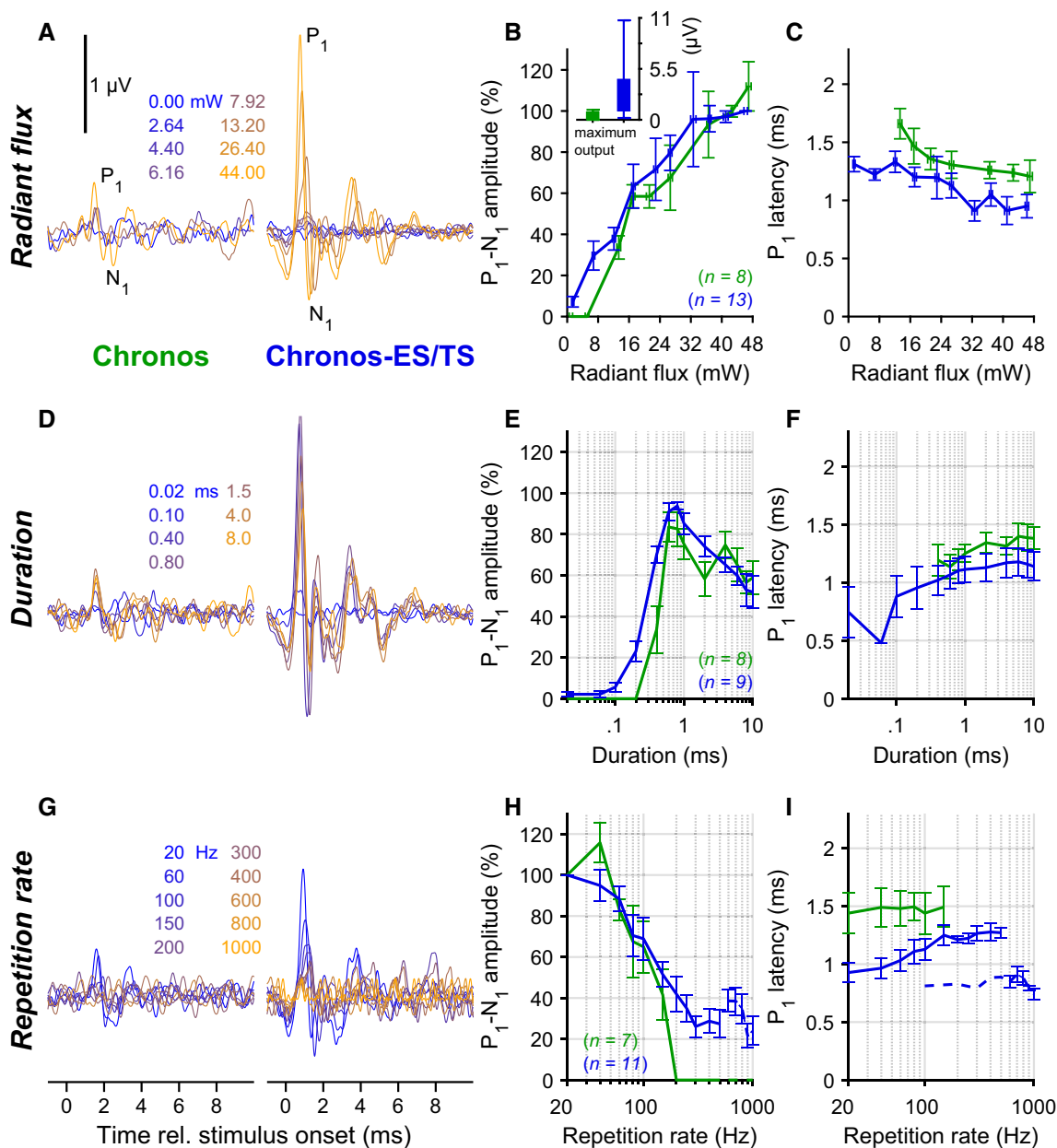


Figure 5. Characterizing optogenetic stimulation by recordings of oABRs.

A oABRs driven with varying radiant flux (1 ms at 10 Hz, colors code the radiant flux in mW) for exemplary mice injected with AAV-PHP.B-Chronos (left) or AAV-PHP.B-Chronos-ES/TS (right).

B Normalized P_1-N_1 amplitude of oABR as a function of light intensity for Chronos as in (A) (green, throughout figure) and Chronos-ES/TS (blue). Radiant flux was binned per 5 mW steps (horizontal error: \pm SEM). Inset: maximal absolute P_1-N_1 amplitude of oABR (mean \pm SEM) was greater for Chronos-ES/TS than for Chronos (Mann-Whitney *U*-test, *P*-value \leq 0.001).

C Latency of oABR P_1 as a function of radiant flux as in (B). Radiant flux was binned per 5 mW steps (horizontal error: \pm SEM).

D oABRs driven with varying stimulus duration (10 Hz, 38 mW, colors code the duration) for exemplary mice injected with AAV-PHP.B-Chronos (left) or AAV-PHP.B-Chronos-ES/TS (right).

E P_1-N_1 amplitude as a function of stimulus duration as in (D) (normalized against the largest P_1-N_1 oABR amplitude).

F Latency of oABR P_1 as a function of stimulus duration as in (E).

G oABRs driven with varying stimulus rate (1 ms and 0.5 ms for 10–500 Hz and 500–1,000 Hz, respectively, 38 mW, colors code the stimulus rate) for exemplary mice injected with AAV-PHP.B-Chronos (left) or AAV-PHP.B-Chronos-ES/TS (right).

H P_1-N_1 amplitude as a function of stimulus rate as in (G) (normalized against P_1-N_1 oABR amplitude at 20 Hz).

I Latency of oABR P_1 as a function of stimulus rate as in (H): Chronos-ES/TS enables responses up to at least 1,000 Hz. Dashed line indicates latencies data points obtained with a pulse duration of 0.5 ms.

Data information: The P_1-N_1 amplitude and P_1 latency were measured on the same animals. Animal count (*n*) is stated on bottom right of panels (B, E and H). Data are expressed as mean \pm SEM.

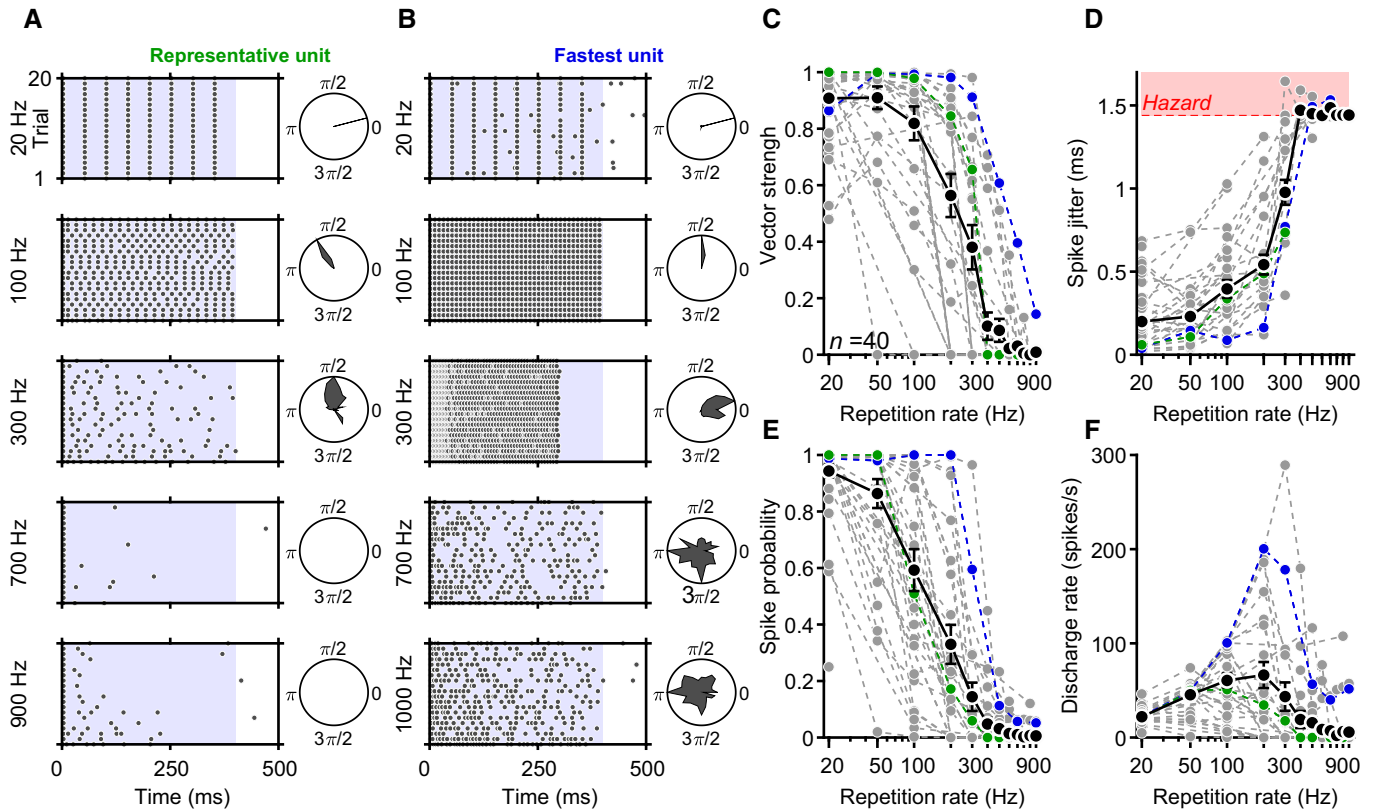


Figure 6. Characterizing optogenetic stimulation by extracellular recordings from single putative SGNs.

A Raster plots showing spiking activity from a representative putative SGN ("unit") in response to 400-ms-long trains of laser pulses (at 30 mW, 1 ms for 20–600 Hz, 500 μ s for ≥ 700 Hz) recorded at five different stimulation rates over 20 repetitions. Polar plots to the right side of raster plots show synchronicity of firing relative to the cycle between two pulse onsets.

B Same protocol and analysis of the "fastest unit" recorded, showing lower adaptation and firing even at very high stimulation rates.

C–F Quantification of the vector strength (C), spike jitter (D), spike probability (E), and discharge rate (F) as a function of repetition rate of 40 putative SGNs (obtained from 6 mice). In panel (D), the red-shaded area represents the hazard function obtained in response to simulated Poisson spike trains.

Data information: Black data points and lines show mean \pm SEM; individual units are shown in gray. The units shown on panels (A and B) are shown in green and blue, respectively. Number of units tested for each repetition rate: 20 Hz: 40, 50 Hz: 25, 100 Hz: 24, 200 Hz: 26, 300 Hz: 21, 400 Hz: 20, 500 Hz: 21, 600 Hz: 18, 700 Hz: 18, 800 Hz: 19, 900 Hz: 21, 1,000 Hz: 19.

SGN) as described in (Hernandez *et al*, 2014; Mager *et al*, 2018). In brief, we targeted glass micropipettes to where the auditory nerve enters the anteroventral cochlear nucleus (AVCN) and searched for responses while stimulating the SGNs through the round window via an optical fiber-coupled to a blue laser. We favored recordings of SGNs by deep positioning ($> 1,000 \mu\text{m}$ relative to the surface of the cochlear nucleus) of the pipette tip, but, given that responses to acoustic stimuli were lost upon the ear surgery, we could not safely discriminate SGNs from AVCN neurons; hence, we termed the light-responsive neurons "putative SGN". We found that the putative SGNs fired upon optogenetic stimulation with high temporal precision for stimulus rates of up to hundreds of Hz (Fig 6A and B); some neurons followed stimulation to some extent even up to 1,000 Hz (Fig 6B). Temporal precision of firing, evaluated based on vector strength (Goldberg & Brown, 1969), see Materials and Methods, Fig 6C) and spike jitter (i.e., standard deviation of spike latency across trials, Fig 6D), was generally high, but varied across the recorded neurons.

Temporal precision and spike probability (Fig 6E) diminished with increasing stimulation rates, indicating that single SGNs code

optogenetic information in a less reliable manner at very high stimulation rates. Spike jitter, calculated for spikes occurring in a time window comprised between two pulse onsets, increased with rate but was typically below a millisecond for stimulus rates lower than 300 Hz (Fig 6D). At higher stimulus rates, spike jitter increased beyond the values obtained for simulated Poisson spike trains (see Materials and Methods, red-shaded area, Fig 6D), indicating that spike synchronization with the light pulses became less reliable. The lower spike precision and limited spike probability at stimulus rates beyond 100 Hz observed are likely compensated by the population response, as several SGNs jointly encode information from each place of the tonotopic map (Lieberman, 1978).

Light-evoked firing rate patterns differed among the putative SGNs as stimulation rates increased (Fig 6F). There was, in general, a linear rise of discharge rates up to 100 Hz, followed by a constant decrease as a response to mid- and high stimulation rates. Nevertheless, some putative SGNs were able to maintain moderate (and to some extent synchronized) spike rates even at pulse rates of 1,000 Hz (fibers showing computable spike probability—see Materials and Methods—at 500 Hz: 7/21, 33.3%; at 600 Hz: 3/18, 16.7%;

at 700 Hz: 3/18, 16.7%; at 800 Hz: 1/19, 5.26%; at 900 Hz: 2/21, 9.52%; and at 1,000 Hz 2/19, 10.53%). Interestingly, the response patterns of the putative SGNs that we recorded varied across units at increasing stimulation rates (Fig EV2). We found two main types of responses: putative SGNs that rapidly adapted their spiking as stimulation rates rose (Fig EV2A) and neurons that continued spiking even at very high pulse rates (albeit with a lower frequency as compared to lower stimulation rates, Fig EV2B).

Discussion

Here, we characterized and optimized Chronos for its utility in fast optogenetic control of excitable cells. We demonstrate sub-millisecond off-kinetics at physiological temperature of Chronos. Using the auditory system as a fast-spiking neural model circuitry, we show that Chronos supports ultrafast control of neuronal spiking. In doing so, we solved a major shortcoming that plagued optogenetics as a stimulus modality for the cochlea, the low temporal fidelity of light-driven SGN firing, caused by the slow deactivation kinetics of the ChR2 employed so far. We found that adding sequences promoting ER-exit and plasma membrane trafficking to Chronos (Chronos-ES/TS) and using postnatal injection of the powerful AAV-PHP.B vector critically improved the *in vivo* utility. In conclusion, Chronos-ES/TS in combination with potent viral vectors such as AAV-PHP.B is a promising tool for auditory neuroscience and a candidate ChR for use in future optical CIs.

Biophysical characterization of Chronos and improving plasma membrane expression

Here, we compared activation and deactivation for ChR2 and Chronos and also studied the temperature dependence of gating for Chronos. In our hands, Chronos deactivates about 3 times faster than ChR2 and has sub-milliseconds off-kinetics at physiological temperature with a Q_{10} of 2.7. This reflects short-lived open states for Chronos resulting in lower open probability, which together with the relatively poor membrane expression likely explains the challenges we faced with using the original Chronos construct for driving SGN spiking, when using the transuterine injection in the AAV2/6-hSyn vector that we previously used successfully for the ChR2 mutant CatCh (Hernandez *et al*, 2014). No problems were reported in two other studies of Chronos in the auditory system using different viruses and stages of the pathway: cochlear nucleus (Hight *et al*, 2015) and inferior colliculus (Guo *et al*, 2015). A recent study using the *in silico* predicted ancient AAV Anc80 also achieves functional expression in the cochlea, but did not differentiate between expression in SGNs and hair cells (Duarte *et al*, 2018). Inspecting the Chronos-GFP expression in the cochlear nucleus (Fig 2 of Hight *et al*, 2015) and SGNs (Duarte *et al*, 2018) suggests a similar diffuse intracellular distribution as we observed in HEK-293T cells (Fig 2) and hippocampal neurons (Fig 3) in culture as well as in SGNs in our study (Fig 4). Using these 3 cell types and vastly different conditions, we show a robust improvement of the plasma membrane expression of Chronos upon adding ER export (Ma *et al*, 2001; Stockklausner *et al*, 2001) and trafficking signals (Hofherr *et al*, 2005) of inward rectifying K^+ channels. Introduction of the powerful AAV-variant AAV-PHP.B (Deverman *et al*, 2016)

was an additional factor *changing the game*: even the unmodified Chronos (Klapoetke *et al*, 2014) enabled oABRs on a regular basis. However, when comparing the functionality of Chronos-ES/TS with enhanced membrane trafficking to Chronos, transduced by the same AAV-PHP.B vector, titer, injection method, and incubation time, we found increased oABR amplitudes and improved temporal fidelity of the Chronos-ES/TS-mediated responses, when increasing the rate of stimulation. Disentangling the contributions of the improved membrane expression and the slightly higher fraction of Chronos-positive SGNs with Chronos-ES/TS is challenging. Regardless of the precise contributions, these experiments suggest that Chronos-ES/TS will be a valuable tool for optogenetic applications requiring good temporal fidelity. Moreover, avoiding the largely intracellular localization of Chronos lowers the proteostatic stress to the cell.

Ultrafast Chronos-mediated stimulation of the auditory pathway

Stimulation of the auditory pathway is a prime example for an application of optogenetics requiring both high speed and light sensitivity. Upon sound stimulation, SGNs fire at hundreds of Hz and show sub-millisecond temporal precision of spiking relative to the stimulus. When considering optogenetics for improved cochlear prosthetics, each stimulus should not exceed the energy requirements of electrical cochlear implants which are in the range of 0.2 μ J per pulse (Zierhofer *et al*, 1995). However, so far, the threshold for optogenetic activation of SGNs reported for ChR2 and ChR2 variant CatCh amounted to approximately 2 μ J, and the responses broke down for stimulation rates exceeding 20 Hz (Hernandez *et al*, 2014).

Chronos, featuring a sub-millisecond deactivation time constant at physiological temperature (Fig 1), is an obvious candidate for cochlear optogenetics. So far, we had employed transuterine AAV2/6-injections into the embryonic otocyst and observed a strong basoapical gradient of expression in the cochlea (Hernandez *et al*, 2014). Using AAV-PHP.B, a novel AAV vector (Deverman *et al*, 2016) at high titers (1–2.5 10^{12} GC/ml) for injections into the cochlea of p5-p7 mice, we found highly efficient transduction of SGNs across all cochlear turns (Fig 5). The light thresholds estimated for oABRs mediated by postnatal AAV-PHP.B injections of Chronos-ES/TS in SGNs amounted to 7 μ J (14 μ J for Chronos), which is substantially higher than the energy per pulse for supra-threshold stimulation in eCIs. Therefore, further improvements of membrane expression of Chronos or the design of fast channels with larger pore remain an important objective. At present, we can only speculate how much light will be required for an auditory percept mediated by Chronos-based cochlear optogenetics. Future studies using behavioral experiments will be required to address this point. Nonetheless, we argue that future optogenetic CIs might not need the high stimulation rates employed in eCIs (800 Hz or higher) which might help balancing a greater energy requirement per pulse of an oCI. In most animals, oABR increased in amplitude when increasing light intensity over more than one order of magnitude (Fig 6). Hence, the output dynamic range of optical stimulation assessed as P_1-N_1 amplitude, on average, was > 10 dB (mW) compared to typically < 10 dB for coding with eCI (Zeng *et al*, 2008). This likely reflects the lower spread of excitation with optical stimulation as well as differences in the levels of Chronos-ES/TS expression among SGNs at the same tonotopic place of stimulation.

The temporal fidelity of Chronos-ES/TS-mediated optogenetic stimulation was estimated at the single SGN and the SGN population levels. The minimal oABR latency was considerably shorter (1.01 ± 0.09 ms) than that of the first light-evoked potential, typically a trough, that we had previously reported for transgenic Chr2 mice (3.14 ± 0.26 ms; Hernandez *et al*, 2014). Moreover, the minimal duration of the light pulse required for eliciting an oABR at high light intensity was shorter (< 100 μ s) than that found before with Chr2 or CatCh (≥ 200 μ s; Hernandez *et al*, 2014). Most importantly, population responses mediated by Chronos-ES/TS followed pulse rates up to at least 1,000 Hz unlike for Chr2, where oABRs were lost below 100 Hz. Obviously, the analysis had to be restricted to a very short measurement time window in order to track the response to such high rates and hence signal propagation along the pathway cannot be demonstrated. This ABR analysis suggests that the Chronos-ES/TS-mediated optogenetic stimulation achieves a temporal fidelity similar to that of acoustic coding. Using juxtacellular recordings, we could demonstrate firing of single SGNs in response to trains of light pulses at hundreds of Hz with sub-millisecond temporal precision. Such temporal fidelity of optogenetic control of SGN firing marks a major breakthrough on the way toward using optogenetic stimulation for auditory research and for the future development of the clinical optical cochlear implant.

Materials and Methods

Cloning

For the cloning of pAAV_hSyn_Chronos-ES/TS as a starting material, we have used pAAV-Ef1a-DIO-eNpHR 3.0-EYFP (Addgene, plasmid nr. #26966). In order to obtain flanked EYFP with ES/TS sequences, we performed a classical PCR. The primers that we used for this cloning were 5'-GAGAACCGGTCAAGAGCAGGATCAC-3' and 5'-GTGGGGTACCCCTTACACCTCGTTCTC-3'. In the second step, the obtained PCR fragment was digested with AgeI/Acc65I (Thermo Scientific, MA, USA) (Acc65I produces compatible cohesive ends as BsrGI) gel extracted (GeneJET Gel Extraction Kit, Thermo Scientific, MA, USA) and further used for ligation. At the same time, the plasmid pAAV_hSyn_Chronos-GFP (Addgene, plasmid no. 59170) was also digested using restriction enzymes AgeI/BsrGI and used as a backbone plasmid. All obtained ligation products were further tested by the means of colony PCR and finally sequenced by external company.

Cell culture and HEK-293T transfection

HEK-293T cells (ATCC, USA) were cultured at 37°C and 5% CO₂ in DMEM (Gibco, USA) supplemented with 10% fetal calf serum (Gibco, Germany) and 1% penicillin/streptomycin (Sigma, Germany). One day prior to transient transfections, the HEK293T cells were seeded on 24-well plates. The day after seeding, cells were transiently transfected with pAAV_hSyn_Chronos-ES/TS or pAAV_hSyn_Chronos using PEI 25,000 MW (Polysciences Inc. USA). Two days after transfection, cells were briefly washed and then fixed with 4% PFA for 10 min. After fixation, cells were mounted with Mowiol (Sigma, Germany) and processed to

confocal/STED imaging. Cells were regularly tested for mycoplasma contamination. No method of cell line authentication was used.

For characterization of gating kinetics, HEK-293T cells were transfected with 3–5 μ g of plasmid DNA encoding a Chr2-YFP or a Chronos-GFP fusion protein via nucleofection using a Lonza nucleofector device and the Amaxa Cell Line Nucleofection Kit V (Lonza, Switzerland; program Q-01), following the manufacturer's instructions. The pcDNA 3.1-Chr2-YFP construct was kindly provided by Ernst Bamberg (MPI for Biophysics, Frankfurt, Germany), and Chronos-GFP was kindly provided by Edward Boyden (MIT, Cambridge, MA). After transfection, the cells were plated on poly-L-lysine coated 10-mm glass coverslips. Electrophysiological characterization was performed 20–30 h after transfection.

Electrophysiology

Transfection success was accessed via fluorescence in an inverted Axiovert 135 TV fluorescence microscope (ZEISS, Germany), equipped with a 40 \times /0.65 N.A. Achromplan objective. Only cells isolated from others and exhibiting clear membrane fluorescence signal were recorded. Whole-cell patch-clamp recordings were made in voltage-clamp mode (-60 mV holding potential) using an EPC 10 USB amplifier (HEKA Elektronik, Germany). Current signals were low-pass-filtered at 3 kHz and digitized at 20 kHz. Patch-pipettes were prepared from PG10165-4 glass capillaries (World Precision Instruments, USA) in a PIP 6 vertical puller (HEKA Elektronik, Germany) and had resistances between 3 and 5 M Ω when filled with the following pipette solution (in mM): 110 NaCl, 10 Na₄-EGTA, 4 MgCl₂, 10 HEPES, and 10 glucose (pH 7.4 and osmolarity between 285 and 290 mOsm). The bath solution contained (in mM): 145 NaCl, 3 KCl, 1 MgCl₂, 2 CaCl₂, 10 HEPES, and 15 glucose (osmolarity between 310 and 315 mOsm and pH 7.35). Series resistance (always < 20 M Ω before compensation) was electronically compensated 60–90%. For recordings at physiological temperature, warm solution was perfused by gravitation in the recording chamber via an HPT-2 in-line heater (ALA Scientific Instruments, USA) controlled by a TC-10 temperature controller (NPI Electronic, Germany). Temperature at the recording chamber was monitored via a thermistor placed in the chamber, and it was maintained at 36 ± 1 °C. Light stimulation was achieved using a 480-nm diode (5 W Luxeon rebel color with Lambertian dome; Philips Lumileds) controlled by a custom-built controller. Stimulation protocols consisted of 1-s-long light steps at different intensities (0.08, 0.14, 0.19, 0.23, 0.27 mW/mm²), with an 11-s-long dark period in between, or a 10-s-long light chirp linearly increasing from 0.1 to 100 (or 500) Hz and maximum amplitude of 0.27 mW/mm² (following a 1-s-long pre-pulse at half maximum intensity). The LED output faithfully followed the voltage command up to at least 5 kHz. Light-elicited currents were analyzed offline in MATLAB 2011b/2014b (MathWorks, USA), Igor Pro 6/7 (Wavemetrics, USA), and OriginPro 7 (OriginLab, USA), and this included the correction of baseline drifts during the 10-s-long chirp recordings. For recordings at 36°C, occasionally spike-like artifacts occurred due to the in-line heater. Those spikes were removed for display purposes in Fig 1.

Dissociation and culture of hippocampal neurons, AAV infection, and immunocytochemistry

E18 pregnant Wistar rats were sacrificed using CO₂, embryos were removed, and heads of embryos were placed in a 10-cm petri dish containing ice-cold dissection media (HBSS (Gibco) + 10 mM Hepes (Gibco)). Brains were removed and collected in fresh dissection medium. Hippocampi were separated from the brain, and meninges were removed. Hippocampi were digested with 2 ml pre-warmed 37°C 0.05% trypsin–EDTA (Gibco, Germany) for 20 min at 37°C. Trypsin was removed, and the tissue was washed three times with 4°C dissection medium. Dissection medium was replaced with 1 ml pre-warmed NB⁺ (Neurobasal with 1X B-27 supplement, 1X Glutamax and penicillin (5,000 U/ml)/streptomycin (5,000 µg/ml); all from Gibco), and tissue was triturated by gentle pipetting. The tissue suspension was filtered through a 100-µm cell strainer (BD Biosciences). Cells were counted using the trypan blue exclusion method and cultured on 12-mm glass coverslips (Thermo Scientific) coated with poly-D-lysine (PDL, Sigma) dissolved in 0.1 M borate buffer, in 24-well plates (CytoOne) at a density of 80,000 hippocampal neurons per cm² in NB⁺ medium in a HeraCell 240i cell culture incubator (Thermo Scientific) at 37°C and 5% CO₂. On DIV 10, neurons were infected with 1 µl AAV2/6 Chronos, AAV2/6 Chronos-ES/TS, or the same constructs packed in PHP.B virus capsid. 72 h after infection, neurons were briefly washed with pre-warmed PBS and then fixed with 4% PFA at RT for 10 min. After fixation and several steps of washing, neurons were subjected to immunocytochemistry (rabbit anti-Map2 primary antibody, 1:1,000, Abcam, and goat anti-rabbit Alexa 555 secondary antibody, 1:1,000, Invitrogen) and later on to confocal microscopy (Leica SP5).

Virus purification

AAVs were generated in HEK-293T cells (ATCC) using polyethyleneimine transfection (25,000 MW, Polysciences, USA) (Gray *et al*, 2011; Deverman *et al*, 2016). In brief, triple transfection of HEK-293T cells was performed using pHelper plasmid (TaKaRa/Clontech), trans-plasmid providing viral capsid PHP.B (generous gift from Ben Deverman and Viviana Gradinaru, Caltech, USA), and cis-plasmid providing Chronos or Chronos-ES/TS (Fig 1A). The cell line was regularly tested for mycoplasma. We harvested viral particles 72 h after transfection from the medium and 120 h after transfection from cells and the medium. Viral particles from the medium were precipitated with 40% polyethylene glycol 8000 (Acros Organics, Germany) in 500 mM NaCl for 2 h at 4°C and then after centrifugation at 4,000 g for 30 min combined with cell pellets for processing. The cell pellets were suspended in 500 mM NaCl, 40 mM Tris, 2.5 mM MgCl₂, pH 8, and 100 U/ml of salt-activated nuclease (Arcticzymes, USA) at 37°C for 30 min. Afterward, the cell lysates were clarified by centrifugation at 2,000 g for 10 min and then purified over iodixanol (Optiprep, Axis Shield, Norway) step gradients (15, 25, 40, and 60%) (Zolotukhin *et al*, 1999; Grieger *et al*, 2006) at 320,006 g for 2.25 h. Viruses were concentrated using Amicon filters (EMD, UFC910024) and formulated in sterile phosphate-buffered saline (PBS) supplemented with 0.001% Pluronic F-68 (Gibco, Germany). Virus titers were measured using AAV titration kit (TaKaRa/Clontech) according to manufacturer's instructions by determining the number of DNase I-resistant vg using qPCR

(StepOne, Applied Biosystems). Purity of produced viruses was routinely checked by silver staining (Pierce, Germany) after gel electrophoresis (Novex™ 4–12% Tris–glycine, Thermo Fisher Scientific) according to manufacturer's instruction. The presence of viral capsid proteins was positively confirmed in all virus preparations. Viral stocks were kept at –80°C until experimental day.

Transuterine AAV injection into the cochlea

For *in vivo* transduction, anesthesia was induced with a mixture of ketamine and xylazine (0.125/5 mg/kg) and maintained with isoflurane (1–2%). Viral inoculum (~250 µl, 4e+8 particles/µl) was microinjected through the uterus into the mouse otocyst from E11.5 to E12.5 as previously described (Brigande *et al*, 2009; Reisinger *et al*, 2011). Only the left otocyst of each embryo was injected. The non-injected contralateral ear served as an internal control. AAV2/6_hSyn_Chronos-GFP and AAV2/6_hSyn_Chronos-ES/TS were purchased from the University of North Carolina Vector Core, Chapel Hill, USA.

Postnatal AAV injection into the cochlea

Postnatal AAV injection into scala tympani of the left ear via the round window was performed at p5–p7 wild-type C57BL/6 mice essentially as described (Akil *et al*, 2012) using AAV-PHP.B viral capsids and hSyn promoter to drive transgenic expression of opsins in SGNs. In brief, under general isoflurane anesthesia and local analgesia achieved by means of xylocaine, the left ear was approached via a dorsal incision and the round window membrane was identified and gently punctured using a borosilicate capillary pipette that was kept in place to inject approximately 1–1.5 µl of AAV2/6_hSyn-Chronos (2.33E+12 GC/ml), AAV2/6_hSyn-Chronos-ES/TS (2.2E+12 GC/ml), PHP.B_hSyn-Chronos-GFP (1.07E+12 GC/ml), or PHP.B_hSyn-Chronos-ES/TS-EYFP (2.31E+12 GC/ml). After virus application, the tissue above the injection site was repositioned and the wound was sutured and buprenorphine (0.1 mg/kg) was applied as pain reliever. Recovery of the animals was then daily tracked. In all experiments, mice were randomly selected for injection. No blinding was possible since injections have to be performed in the left ear leaving the right ear as an internal control. Hence, surgery prior to stimulation needed to be done in the injected ear. Animals were then kept in a 12-h light/dark cycle, with access to food and water *ad libitum*. All experiments were done in compliance with the national animal care guidelines and were approved by the board for animal welfare of the University Medical Center Goettingen and the animal welfare office of the state of Lower Saxony. The calculation of animal number was performed prior to starting experiments. We planned to use the Wilcoxon rank-sum test and an error probability alpha smaller than 0.05, a power (1-beta) of 0.95, and effect size depending on the precise experimental protocol.

Immunostaining and imaging of cochlear cryosections

Cochleae were fixed with 4% paraformaldehyde in phosphate-buffered saline (1 h). Sections of the cochlea were cryosectioned following 0.12 M EDTA decalcification. After incubation of sections for 1 h in goat serum dilution buffer (16% normal goat serum, 450 mM NaCl, 0.6% Triton X-100, 20 mM phosphate buffer, pH 7.4), primary antibodies were applied overnight at 4°C. The

following antibodies were used: chicken anti-GFP (catalog n.: ab13970, Abcam, 1:500) and guinea pig anti-parvalbumin (catalog no.: 195004, Synaptic Systems, 1:300). Secondary AlexaFluor-labeled antibodies (goat anti-chicken 488 IgG (H+L), catalog no.: A-11039, Thermo Fisher Scientific, 1:200; goat anti-guinea pig 568 IgG (H+L), catalog no. A1107, Thermo Fisher Scientific, 1:200) were applied for 1 h at room temperature. Confocal images were collected using an SP5 microscope (Leica) and processed in ImageJ. Expression was considered positive when FP fluorescence in a given cell (marked by parvalbumin) was found to be higher than 3 SD above the background fluorescence of the tissue.

For FP localization analysis, line profiles (length: 7.5 μm , 7.5 μm , and 1.5 μm for SGNs, HEK cells, and hippocampal neurons, respectively, width: three pixels) were centered to the outer edge of the estimated cell membrane. The line profiles were oriented perpendicular to the cell edge. Sample size was 1, 1, and 3 per cell for SGNs, HEK cells, and hippocampal neurons, respectively. For membrane/intracellular expression ratio, a maximum peak detection was performed for membranous area (defined positionally on the line profiles as -1 to 1 μm , -1 to 1 μm and -0.5 to 0.3 μm for SGNs, HEK cells, and hippocampal neurons, respectively) and for intracellular area (defined positionally on the line profiles as 1.1 to 2 μm , 1.1 to 2 μm , and 0.4 to 0.5 μm for SGNs, HEK cells, and hippocampal neurons, respectively).

STED microscopy

Images were acquired using an Abberior Instruments Expert Line STED microscope, with excitation lasers at 488 nm and STED lasers at 595 nm, 1 W using a 1.4 NA 100 \times oil immersion objective, either in confocal or in 2D-STED mode.

Optical stimulation *in vivo*

The left bulla was reached using a retroauricular approach and opened to expose the cochlea. A 50/200- μm optical fiber-coupled to a 473-nm laser (MLL-FN-473-100, 100 mW, diode pumped solid state [DPSS]; Changchun New Industry Optoelectronics)[#] was inserted into the cochlea via the round window. Irradiance was calibrated with a laser power meter (LaserCheck; Coherent Inc.).

Auditory brainstem responses

For stimulus generation and presentation, data acquisition, and offline analysis, we used an NI System and custom-written MATLAB software (The MathWorks, Inc.). Optically evoked ABRs (oABRs) and acoustically evoked ABRs (aABRs) were recorded by needle electrodes underneath the pinna, on the vertex, and on the back near the legs. The difference potential between vertex and mastoid subdermal needles was amplified using a custom-designed amplifier, sampled at a rate of 50 kHz for 20 ms, filtered (300–3,000 Hz), and averaged across 1,000 and 500 presentations (for oABRs and aABRs, respectively). The first ABR wave was detected semi-automatically with a custom-written MATLAB script in which the wave was detected for each trace in a temporal window defined by the user and for which the amplitude was bigger than

the average + 2 standard deviations. Thresholds were determined by visual inspection as the minimum sound or light intensity that elicited a reproducible response waveform in the recorded traces.

Juxtacellular recordings from single putative SGNs

For auditory nerve recordings, glass microelectrodes (~ 50 M Ω) were advanced through the posterior end of the anteroventral cochlear nucleus using an Inchworm micro-positioner (EXFO Burleigh, NY, USA) and aimed toward the internal auditory canal. Action potentials were amplified using an ELC-03XS amplifier (NPI Electronic, Tamm, Germany), filtered (300–3,000 Hz), digitized (National Instruments card PCIe-6323), analyzed, and prepared for display using custom-written MATLAB (The MathWorks, Inc.) software. When light-responsive fibers were found, 400-ms-long pulse trains at repetition rates 20–1,000 Hz were presented, leaving 100 ms inter-train recovery over 20 iterations for each tested rate. Different rates were tested following no particular order, being 20 Hz the first repetition rate presented across all units. For repetition rates higher or equal to 200 Hz, parameters were computed if the spike probability was equal or superior to 5%. If not, values were set to 0. Phase-locking was quantified using the vector strength (Goldberg & Brown, 1969), considering a cycle starting at the onset of a light pulse and ending at the onset of the subsequent pulse, and conform-

ing to the equation: vector strength = $\frac{\sqrt{[\sum_{i=1}^n \cos \theta_i]^2 + [\sum_{i=1}^n \sin \theta_i]^2}}{n}$, being $\Theta_1, \Theta_2, \dots, \Theta_n$ cycle phases in which spikes occurred. The Rayleigh test was used to evaluate the significance of vector strength: if $L > 13.8$, the null hypothesis is rejected at the 0.001 significance level (Hillery & Narins, 1987) and insignificant VS were set to 0. The spike probability was calculated as the ratio between the number of spikes and the number of light pulses. The temporal jitter is the standard deviation of spike latency across trials. The hazard function (for the temporal jitter analysis) was calculated for each stimulation rate by simulating spiking as a Poisson process at given rates (from 10 to 1,000 spikes/s).

Data analysis

The data were analyzed using MATLAB (MathWorks), Excel (Microsoft), Igor Pro (Wavemetrics), FIJI (ImageJ2), Origin (Microcal software), and GraphPad Prism (GraphPad software). Averages were expressed as mean \pm SEM or mean \pm SD, as specified. References to data in the main text were expressed as mean \pm SEM. For statistical comparison between two groups, data sets were tested for normal distribution (the D'Agostino & Pearson omnibus normality test or the Shapiro–Wilk test) and equality of variances (F -test) followed by two-tailed unpaired Student's t -test, or the unpaired two-tailed Mann–Whitney U -test when data were not normally distributed and/or variance was unequal between samples.

For evaluation of multiple groups, statistical significance was calculated by using one-way ANOVA test followed by Tukey's test for normally distributed data (equality of variances tested with the Brown–Forsythe test) or one-way Kruskal–Wallis test followed by Dunn's test for non-normally distributed data.

[#]Correction added on 13 November 2018 after first online publication: The laser information was corrected.

Expanded View for this article is available online.

Acknowledgements

We would like to thank Dr. Edward Boyden for providing the Chronos-EGFP construct and Rachel Care for contributing in the initial phase of the project. We thank Andrea Koch, Daniela Gerke, Sandra Gerke, and Christiane Senger-Freitag for expert technical assistance and Gerhard Hoch for devising hard and software for system physiology and Jakob Neef for the help with STED microscopy. We thank Camin Dean for providing hippocampal neuronal culture. We thank Blanche Schwappach for feedback on the manuscript. This work was funded by the European Research Council through the Advanced Grant “OptoHear” to T.M. under the European Union’s Horizon 2020 Research and Innovation program (grant agreement No. 670759) and was further supported by the German Ministry of Research and Education through the Bernstein Center for Computational Neuroscience to A.N., F.W., and T.M. (under grant number 01GQ1005A) and the grant Optical CI (under grant number 13N13729) to T.M.) and the German Research Foundation (through the DFG-Research Center (FZT103) and Cluster of Excellence (EXC171) Center for Nanoscale Microscopy and Molecular Physiology of the Brain to T.M., as well as the Leibniz Program to T.M.).

Author contributions

DK, VR, FW, AN, and TM designed the study. DK performed o/aABR recordings, immunohistochemistry, and FP expression analysis. AG, TD, and CW performed initial o/aABR recordings. RMM performed patch-clamp recordings, BB performed immunohistochemistry. SS and DLM performed initial cloning. VR performed AAV injections, HEK293T and hippocampal neuron experiments, confocal and STED microscopy, and cloning and production of the viruses. DLM performed recordings from single SGNs and oABRs. ATH developed analysis toolboxes for ABRs and recordings from single SGNs and performed analysis of electrophysiological data. All authors analyzed data and contributed to the writing of the manuscript. TM, DK, VR, and AN took a lead on preparing the manuscript.

Conflict of interest

The authors declare that they have no conflict of interest.

References

- RST-001 Phase I/II Trial for Advanced Retinitis Pigmentosa - Full Text View - ClinicalTrials.gov Available at: <https://clinicaltrials.gov/ct2/show/NCT02556736> [Accessed February 20, 2018]
- Adamantidis A, Arber S, Bains JS, Bamberg E, Bonci A, Buzsáki G, Cardin JA, Costa RM, Dan Y, Goda Y, Graybiel AM, Häusser M, Hegemann P, Huguenard JR, Insel TR, Janak PH, Johnston D, Josselyn SA, Koch C, Kreitzer AC et al (2015) Optogenetics: 10 years after ChR2 in neurons—views from the community. *Nat Neurosci* 18: 1202–1212
- Akil O, Seal RP, Burke K, Wang C, Alemi A, During M, Edwards RH, Lustig LR (2012) Restoration of hearing in the VGLUT3 knockout mouse using virally mediated gene therapy. *Neuron* 75: 283–293
- Boyden ES, Zhang F, Bamberg E, Nagel G, Deisseroth K (2005) Millisecond-timescale, genetically targeted optical control of neural activity. *Nat Neurosci* 8: 1263–1268
- Brigande JV, Gubbels SP, Woessner DW, Jungwirth JJ, Bresee CS (2009) Electroporation-mediated gene transfer to the developing mouse inner ear. *Methods Mol Biol* 493: 125–139
- Buskamp V, Picaud S, Sahel JA, Roska B (2012) Optogenetic therapy for retinitis pigmentosa. *Gene Ther* 19: 169–175
- Deverman BE, Pravdo PL, Simpson BP, Kumar SR, Chan KY, Banerjee A, Wu W-L, Yang B, Huber N, Pasca SP, Gradinaru V (2016) Cre-dependent selection yields AAV variants for widespread gene transfer to the adult brain. *Nat Biotechnol* 34: 204–209
- Duarte MJ, Kanumuri VV, Landegger LD, Tarabichi O, Sinha S, Meng X, Hight AE, Kozin ED, Stankovic KM, Brown MC, Lee DJ (2018) Ancestral adeno-associated virus vector delivery of opsins to spiral ganglion neurons: implications for optogenetic cochlear implants. *Mol Ther* 26: 1931–1939
- Goldberg JM, Brown PB (1969) Response of binaural neurons of dog superior olivary complex to dichotic tonal stimuli: some physiological mechanisms of sound localization. *J Neurophysiol* 32: 613–636
- Gradinaru V, Zhang F, Ramakrishnan C, Mattis J, Prakash R, Diester I, Goshen I, Thompson KR, Deisseroth K (2010) Molecular and cellular approaches for diversifying and extending optogenetics. *Cell* 141: 154–165
- Gray SJ, Choi VW, Asokan A, Haberman RA, McCown TJ, Samulski RJ (2011) Production of recombinant adeno-associated viral vectors and use in *in vitro* and *in vivo* administration. *Curr Protoc Neurosci* 57: 4.17.1–4.17.30
- Grieger JC, Choi VW, Samulski RJ (2006) Production and characterization of adeno-associated viral vectors. *Nat Protoc* 1: 1412–1428
- Guo W, Hight AE, Chen JX, Klapoetke NC, Hancock KE, Shinn-Cunningham BG, Boyden ES, Lee DJ, Polley DB (2015) Hearing the light: neural and perceptual encoding of optogenetic stimulation in the central auditory pathway. *Sci Rep* 5: 10319
- Hernandez VH, Gehrt A, Reuter K, Jing Z, Jeschke M, Mendoza Schulz A, Hoch G, Bartels M, Vogt G, Garnham CW, Yawo H, Fukazawa Y, Augustine GJ, Bamberg E, Kügler S, Salditt T, de Hoz L, Strenzke N, Moser T (2014) Optogenetic stimulation of the auditory pathway. *J Clin Invest* 124: 1114–1129
- Hight AE, Kozin ED, Darrow K, Lehmann A, Boyden E, Brown MC, Lee DJ (2015) Superior temporal resolution of Chronos versus channelrhodopsin-2 in an optogenetic model of the auditory brainstem implant. *Hear Res* 322: 235–241
- Hillery CM, Narins PM (1987) Frequency and time domain comparison of low-frequency auditory fiber responses in two anuran amphibians. *Hear Res* 25: 233–248
- Hofherr A, Fakler B, Klöcker N (2005) Selective Golgi export of Kir2.1 controls the stoichiometry of functional Kir2.x channel heteromers. *J Cell Sci* 118: 1935–1943
- Jeschke M, Moser T (2015) Considering optogenetic stimulation for cochlear implants. *Hear Res* 322: 224–234
- Jung S, Maritzen T, Wichmann C, Jing Z, Neef A, Revelo NH, Al-Moyed H, Meese S, Wojcik SM, Panou I, Bulut H, Schu P, Ficner R, Reisinger E, Rizzoli SO, Neef J, Strenzke N, Haucke V, Moser T (2015) Disruption of adaptor protein 2 μ (AP-2 μ) in cochlear hair cells impairs vesicle reloading of synaptic release sites and hearing. *EMBO J* 34: 2686–2702
- Kim CK, Adhikari A, Deisseroth K (2017) Integration of optogenetics with complementary methodologies in systems neuroscience. *Nat Rev Neurosci* 18: 222–235
- Klapoetke NC, Murata Y, Kim SS, Pulver SR, Birdsey-Benson A, Cho YK, Morimoto TK, Chuong AS, Carpenter EJ, Tian Z, Wang J, Xie Y, Yan Z, Zhang Y, Chow BY, Surek B, Melkonian M, Jayaraman V, Constantine-Paton M, Wong GK-S et al (2014) Independent optical excitation of distinct neural populations. *Nat Methods* 11: 338–346
- Kral A, Hartmann R, Mortazavi D, Klinke R (1998) Spatial resolution of cochlear implants: the electrical field and excitation of auditory afferents. *Hear Res* 121: 11–28

- Lalwani AK, Walsh BJ, Reilly PG, Muzyczka N, Mhatre AN (1996) Development of *in vivo* gene therapy for hearing disorders: introduction of adeno-associated virus into the cochlea of the guinea pig. *Gene Ther* 3: 588–592
- Lenarz T (2018) Cochlear implant – state of the art. *GMS Curr Top Otorhinolaryngol Head Neck Surg* 16: Doc04
- Liberman MC (1978) Auditory-nerve response from cats raised in a low-noise chamber. *J Acoust Soc Am* 63: 442–455
- Ma D, Zerangue N, Lin Y-F, Collins A, Yu M, Jan YN, Jan LY (2001) Role of ER export signals in controlling surface potassium channel numbers. *Science* 291: 316–319
- Mager T, Lopez de la Morena D, Senn V, Schlotte J, D'Errico A, Feldbauer K, Wrobel C, Jung S, Bodensiek K, Rankovic V, Browne L, Huet A, Jüttner J, Wood PG, Letzkus JJ, Moser T, Bamberg E (2018) High frequency neural spiking and auditory signaling by ultrafast red-shifted optogenetics. *Nat Commun* 9: 1750
- Mardinly AR, Oldenburg IA, Pégard NC, Sridharan S, Lyall EH, Chesnov K, Brohawn SG, Waller L, Adesnik H (2018) Precise multimodal optical control of neural ensemble activity. *Nat Neurosci* 21: 881–893
- Nagel G, Ollig D, Fuhrmann M, Kateriya S, Musti AM, Bamberg E, Hegemann P (2002) Channelrhodopsin-1: a light-gated proton channel in green algae. *Science* 296: 2395–2398
- Nagel G, Szellas T, Huhn W, Kateriya S, Adeishvili N, Berthold P, Ollig D, Hegemann P, Bamberg E (2003) Channelrhodopsin-2, a directly light-gated cation-selective membrane channel. *Proc Natl Acad Sci USA* 100: 13940–13945
- Reisinger E, Bresee C, Neef J, Nair R, Reuter K, Bulankina A, Nouvian R, Koch M, Buckers J, Kastrop L, Roux I, Petit C, Hell SW, Brose N, Rhee J-S, Kugler S, Brigande JV, Moser T (2011) Probing the functional equivalence of otoferlin and synaptotagmin 1 in exocytosis. *J Neurosci* 31: 4886–4895
- Richter C-P, Rajguru SM, Matic AI, Moreno EL, Fishman AJ, Robinson AM, Suh E, Walsh JT (2011) Spread of cochlear excitation during stimulation with pulsed infrared radiation: inferior colliculus measurements. *J Neural Eng* 8: 056006
- Sahel J-A, Roska B (2013) Gene therapy for blindness. *Annu Rev Neurosci* 36: 467–488
- Stockklauser C, Ludwig J, Ruppertsberg JP, Klöcker N (2001) A sequence motif responsible for ER export and surface expression of Kir2.0 inward rectifier K(+) channels. *FEBS Lett* 493: 129–133
- WHO (2018) *Deafness and hearing loss*. <http://www.who.int/news-room/factsheets/detail/deafness-and-hearing-loss>
- Wrobel C, Dieter A, Huet A, Keppeler D, Duque-Afonso CJ, Vogl C, Hoch G, Jeschke M, Moser T (2018) Optogenetic stimulation of cochlear neurons activates the auditory pathway and restores auditory-driven behavior in deaf adult gerbils. *Sci Transl Med* 10: eaao0540
- Zeng F-G, Rebscher S, Harrison WV, Sun X, Feng H (2008) Cochlear implants: system design, integration and evaluation. *IEEE Rev Biomed Eng* 1: 115–142
- Zeng FG (2017) Challenges in improving cochlear implant performance and accessibility. *IEEE Trans Biomed Eng* 64: 1662–1664
- Zierhofer CM, Hochmair-Desoyer IJ, Hochmair ES (1995) Electronic design of a cochlear implant for multichannel high-rate pulsatile stimulation strategies. *IEEE Trans Rehabil Eng* 3: 112–116
- Zolotukhin S, Byrne BJ, Mason E, Zolotukhin I, Potter M, Chesnut K, Summerford C, Samulski RJ, Muzyczka N (1999) Recombinant adeno-associated virus purification using novel methods improves infectious titer and yield. *Gene Ther* 6: 973–985